

A hybrid 2-stage vision transformer for AI-assisted 5 class pathologic diagnosis of gastric endoscopic biopsies

Yujin Oh¹, Go Eun Bae², Kyung-Hee Kim³, Min-Kyung Yeo^{†,2}, Jong Chul Ye^{†,1}

¹Kim Jaechul Graduate School of Artificial Intelligence, KAIST, Daejeon, Republic of Korea

²Department of Pathology, Chungnam National University School of Medicine, Chungnam National University Hospital, Daejeon, Republic of Korea

³Department of Pathology, Chungnam National University School of Medicine, Chungnam National University Sejong Hospital, Sejong, Republic of Korea

[†]Correspondence should be addressed to Min-Kyung Yeo (mkyeo83@cnu.ac.kr) and Jong Chul Ye (jong.ye@kaist.ac.kr)

Abstract

Gastric endoscopic screening is an effective way to decide appropriate gastric cancer (GC) treatment at an early stage, reducing GC-associated mortality rate. Although artificial intelligence (AI) has brought a great promise to assist pathologist to screen digitalized whole slide images, automatic classification systems for guiding proper GC treatment based on clinical guideline are still lacking. Here, we propose an AI system classifying 5 classes of GC histology, which can be perfectly matched to general treatment guidance. The AI system, mimicking the way pathologist understand slides through multi-scale self-attention mechanism using a 2-stage Vision Transformer, demonstrates clinical capability by achieving diagnostic sensitivity of above 85% for both internal and external cohort analysis. Furthermore, AI-assisted pathologists showed significantly improved diagnostic sensitivity by 10% within 18% saved screening time compared to human pathologists. Our AI system has a great potential for providing presumptive pathologic opinion for deciding proper treatment for early GC patients.

Gastric cancer (GC) is reported as the fourth most leading cause of cancer death worldwide¹. Endoscopic screening is an effective way to detect GC at an early stage, guiding patients to get appropriate treatment according to the cancer stage. Although gastric endoscopic screening and proper early treatment has reduced GC-associated mortality rate², the increasing number of GC screenings and endoscopic biopsy slides adds an additional diagnostic workload to the limited number of clinical resources. Accordingly, emerging application of artificial intelligence (AI) for digital pathology has brought a great opportunity to effectively reduce diagnostic overloads, by utilizing massive number of digitalized whole slide images (WSIs). AI has already achieved powerful cancer diagnostic performance on various organs, such like prostate and breast cancer³⁻⁵.

Recently, several AI-assistance systems have been developed for automatic GC diagnosis⁶⁻¹⁰. However, previous studies mostly focused on providing screening tool to detect malignancy over benign or classifying gastric adenoma and carcinoma cases, limiting their practical usage to closely cover clinical pathology diagnosis. Herein, we classify gastric endoscopic biopsied pathologic diagnosis into 5 categories as follows: negative for dysplasia (NFD), tubular adenoma (TA), differentiated carcinoma (Diff-CA), undifferentiated carcinoma (Undiff-CA), and MALT lymphoma (MALT), which can assist clinician to guide proper GC treatment for the early gastric lesion in the clinical setting (Table. 1)¹¹.

Most AI-assistance systems for GC diagnosis adapt convolutional neural network (CNN)⁶⁻¹⁰. Since CNN is limited in expanding its input receptive field to cover gigapixel-level WSIs, patch-level training has become widespread by dividing WSIs into sub-patches¹². However, the patch-wise training is not effective in exploiting the inter-patch structural relationship. In fact, GC histology classification needs comprehensive information of cell to tissue-level morphological structure. In particular, when confusing cases exist in borderlines between two adjacent classes, pathologists review slides by switching magnification from low to high resolution to understand both global structural relationships and regional morphology. To mimic the way how pathologist

understand WSIs, Park and colleagues proposed a RACNN to expand receptive field by aggregating patch-level features using additional convolution layers⁸. However, the additional convolution layers still limit comprehensive understanding of inter-patch relationship for effective global to local analysis.

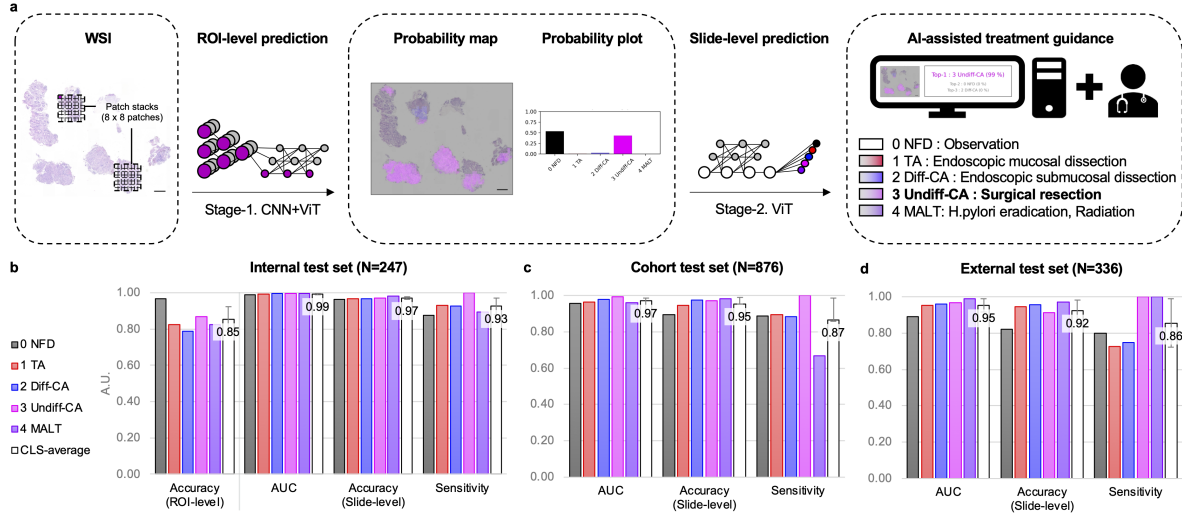


Figure 1: The schematic of our AI system and model performance. (a) Overview of 2-stage AI-assisted gastric cancer treatment guidance system. The AI system is composed of two stages of ViT modules, for ROI-level and slide-level. The slide-level prediction can be matched to general treatment guidance. (b)-(d) Class-wise and class-average performance plot of the AI system for three different test set.

To address this, inspired by the success of Vision Transformer (ViT)¹³ that exploit long-range dependency among non-adjacent patches through attention mechanism, here we propose a hybrid CNN and ViT framework that can significantly expand receptive field and reflect the way pathologist diagnose WSIs. Specifically, as illustrated in Fig. 1a, our system is composed of two stages of ViT: the first stage ViT receives features from CNN layers to obtain ROI-level prediction, which is followed by the second stage ViT for the slide-level prediction. Specifically, multiple patch stacks from each WSI are fed into the the region-of-interest (ROI)-level network to be trained to match their corresponding patch-level annotations. The ROI-level inference results over entire WSI are then fed into the slide-level network and trained to match its corresponding diagnosis. As a whole, we can build up patch stacks consisted of 8×8 grid of sub-patches to expand receptive field

up to 1×1 mm for ROI-level prediction, and up to entire size of WSI for slide-level prediction. In this way, the proposed AI system mimic the entire process how pathologist understand WSI.

Our AI system demonstrates its capability of multi-class GC histology classification by achieving average diagnostic sensitivity of 0.87 ± 0.12 on daily acquired gastric cohort test set. The AI system also demonstrates its great generalizability on the external cohort test set by achieving average sensitivity of 0.86 ± 0.13 , which is comparable to internal cohort test. Furthermore, in the observation study, pathologists assisted by the AI system shows significantly improved diagnostic performance by achieving average diagnostic sensitivity of 0.93 ± 0.06 at shorter screening time compared to human pathologist performance of 0.83 ± 0.03 . The reliable performance of the AI system on multi-center daily cohorts and its clinical capability demonstrates that our AI system holds great promise in providing practical opinion for guiding appropriate treatment for early GC patients.

Results

AI system training and internal test. The internal dataset was collected from Chungnam National University Hospital (CNUH). The internal train and validation set included 1,228 WSIs from endoscopic biopsy slides. One clear WSI per each slides was collected automatically and utilized with down-sampled WSIs at x20 magnification with resolution of $0.49 \mu m$ per pixel for further training and evaluation. For the convenience of training the AI system, WSIs were split into 2048×2048 -pixel patch stacks. Patch stacks were sampled from all the train set and maximum 100 patch stacks were collected from each WSI depending on its size. Patch stacks containing foreground tissues below 30 percentile to the entire patch stack size were excluded from the train set.

The internal dataset was randomly split into training, validation, and internal test sets, each

consisting of 70, 10, and 20 percent of the total dataset. Specifically, our model was trained by using total 12,510 patches from 846 WSIs, and validated on 135 WSIs. Then, the model was evaluated on internal test set of 247 WSIs. A detailed dataset information is provided in Supplementary Table S1a.

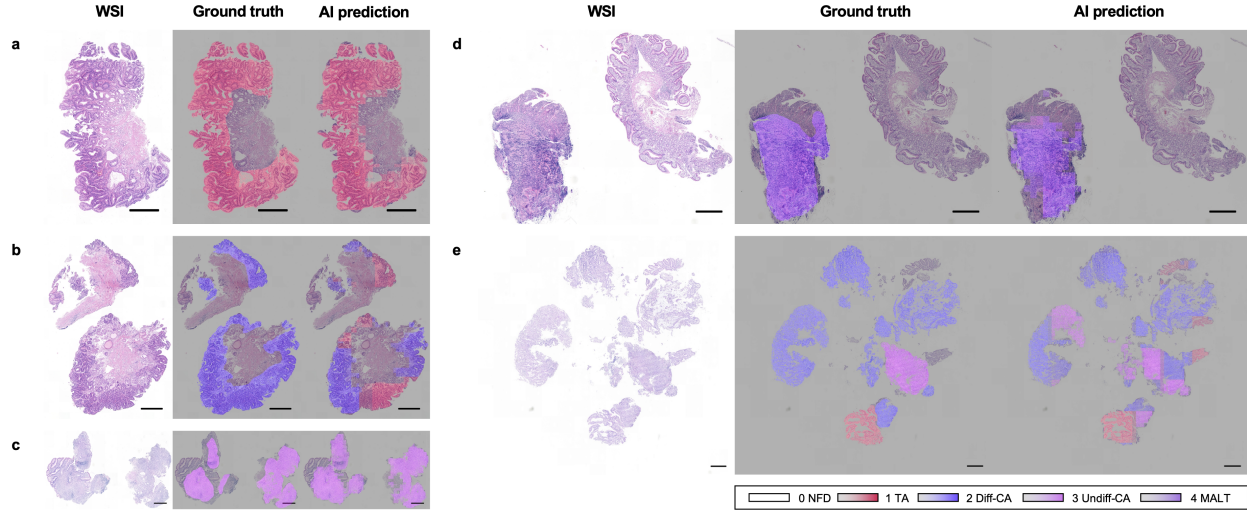


Figure 2: ROI-level probability map. Representative cases selected from (a) TA, (b) Diff-CA, (c) Undiff-CA, (d) MALT and (e) Undiff-CA. All the scale bars indicate 500 μm .

For the internal data set, our model achieved ROI-level accuracy over 0.85 (macro average over 5 classes), as plotted in Fig. 1b. The probability map highly corresponds to the ground truth annotation, as shown in Fig. 2. A close analysis showed that our model was mostly confused when distinguishing between TA/Diff-CA (see Fig. 2b), due to their patch-level morphological similarity. For slide-level prediction, the AI system correctly classified most of cases (229 of 247 cases) and achieved the average area under the curve (AUC) of 0.99 ± 0.00 (accuracy of 0.97 ± 0.01 and sensitivity of 0.93 ± 0.05). Most error cases were counted when distinguishing between adjacent classes (9 of 247 cases) and false-positive cases of NFD (9 of 73 cases). Slide-level confusion matrix and a representative result of WSI falsely diagnosed are shown in Fig. 3a-c. The representative result contains ROI-level probabilities of multiple classes, thus slide-level prediction is uncertain with probability of under 90%. Detailed metrics are provided in Supplementary Table S2a.

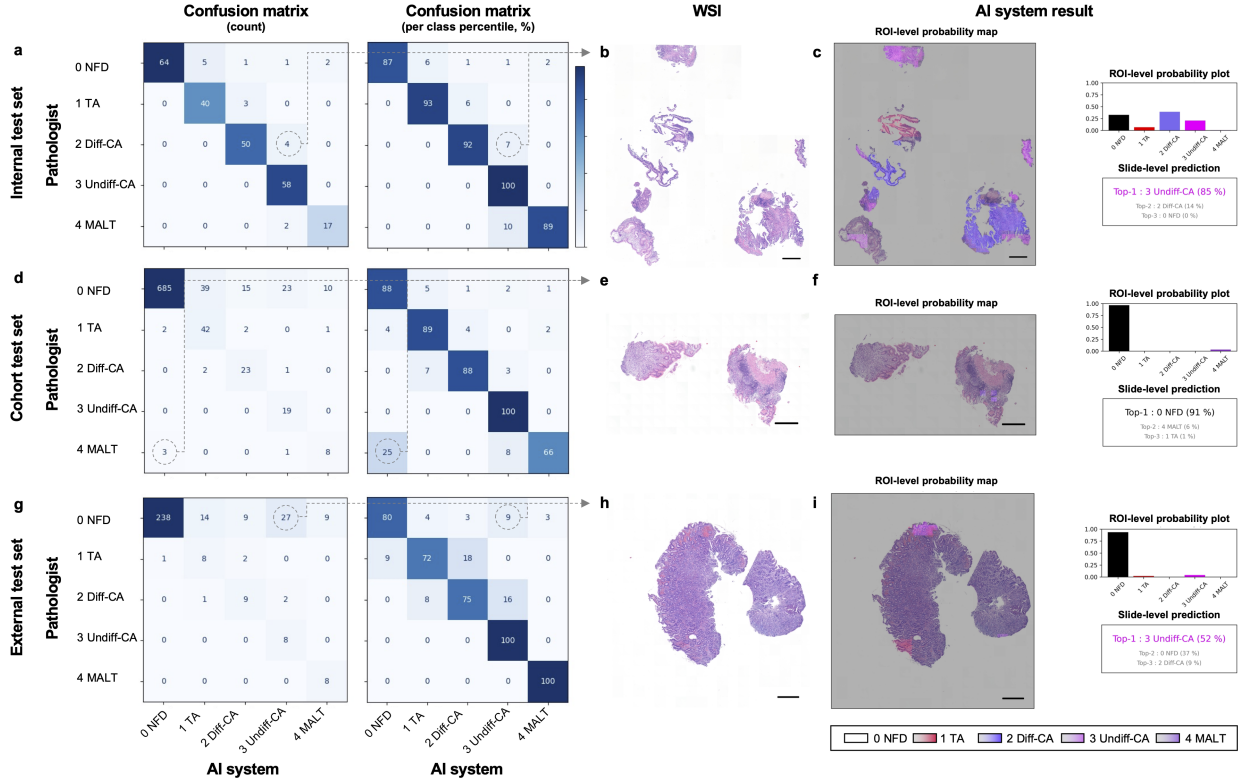


Figure 3: Slide-level prediction performance. (a), (d), (g) Confusion matrix of the AI system and the corresponding case-wise prediction results for three different test set. (b)-(c), (e)-(f), (h)-(i) A representative case selected from class with high error rate from three different test set, respectively. The dotted lines indicate corresponding classes each representative cases selected from. All the scale bars indicate 500 μm .

Cohort test. The AI system was further evaluated on daily gastric endoscopic screening cohort set acquired from CNUH. The cohort test set included 876 WSIs from endoscopic biopsy slides cohort from June 2021 to July 2021. A detailed dataset is described in Supplementary Table. S1c.

The AI system correctly classified most of cases (777 of 876 cases) and achieved comparable performance to the internal test set with AUC of 0.97 ± 0.02 (accuracy of 0.95 ± 0.04 and sensitivity of 0.87 ± 0.12) as plotted in Fig. 1c. Similar to the internal test results, most error cases were counted when distinguishing between adjacent classes (8 of 104 cases) and false-positive cases of NFD (87 of 772 cases). Detailed dataset information and metrics are provided in Supplementary Table S1b and S2b, respectively.

In contrast to the internal test results, errors cases were also counted when discriminating non-adjacent classes between NFD/MALT (3 of 12 cases) and TA/MALT (1 of 47 cases), as shown in Fig. 3d. For analyzing error cases which not occurred in the internal test set, we randomly sampled at most 30 cases per classes from the cohort test set and performed thorough analysis. As summarized in Fig 4a, we stratified diagnostic difficulty into 4 levels following previous trial ⁶: level 1, easy to diagnose under low magnification; level 2, easy, but needed examination under high magnification; level 3, difficult, but ancillary test not required; level 4, challenging and ancillary test required. On the sampled cohort test set, the AI system showed accuracy of above 0.90 for cases ranked as diagnostic difficulty level 1 to 2, whereas, accuracy decreased to 0.63 and 0.55 as difficulty level increased to 3 and 4, respectively. Above 4 error cases counted from non-adjacent borderline were ranked as difficulty level 3 or 4.

Specifically, MALT class consists of above 30% (4 of 12 cases) cases required ancillary test, which ranked as diagnostic difficulty level 4. Fig. 3e-f depicts a representative case falsely diagnosed as negative for MALT class. The ROI-level probability map includes small portion of patches diagnosed as MALT class and under-estimated ROI-level probability. The results indicate that the AI system shows poor performance on slides that need ancillary test for accurate diagnosis.

External test. The AI system was further evaluated on external cohort dataset for validating its generalizability for multi-centre dataset. The external dataset was collected from Chungnam National University Sejong Hospital (CNUSH), including 336 WSIs from endoscopic biopsy slides cohort from September 2020 to February 2021. A detailed dataset distribution is described in Supplementary Table. S1c.

On 336 WSIs, the AI system achieved comparable performance to the cohort test set with AUC of 0.95 ± 0.04 (accuracy of 0.92 ± 0.06 and sensitivity of 0.86 ± 0.13) as plotted in Fig. 1d. Detailed external test set and performance are provided in Supplementary Table S1c and S2c,

respectively. All the error cases were counted when distinguishing between adjacent classes (6 of 39 cases) except for false-positive cases of NFD (59 of 297 cases), similar to the internal test results. Slide-level confusion matrix and a representative result of WSI falsely diagnosed are shown in Fig. 3g-i. The ROI-level probability for the falsely-classified class is below 0.1, thus slide-level prediction is uncertain with probability score below 60%.

False-positive cases. In the internal test set and cohort test set, 4% (9 of 247 cases) and 10% (87 of 876 cases) of false-positive cases to entire dataset were observed, respectively. The falsely classified as non-NFD by detailed classification are summarized in Supplementary Table S3a. In the detailed NFD classes, hyperplastic polyp showed the highest false-positive rate of 19%, followed by acute and atrophic gastritis with 17% and 8%, respectively, whereas, 0% for foveolar hyperplasia.

In the external test set, 18% (59 of 336 cases) of false-positive cases to entire dataset were observed. As summarized in Supplementary Table S3b, acute gastritis showed the highest false-positive rate of 31%, followed by hyperplastic polyp and atrophic gastritis with 20% and 12%, respectively. Similar to the cohort test set, foveolar hyperplasia showed no false-positive case.

Observer test. The practical usability of the AI system on daily gastric endoscopic screening was evaluated on observation of AI-assisted pathologist performance. Total 6 pathologists were asked to diagnosis 2 observer test set (N=25/set) within identical time constraints for each set. All the observer test set were curated with balanced distribution of class and diagnostic difficulty level. Half of the pathologists were asked to diagnose WSIs without AI-assistance (Pathologist-only trial) for the former test set and then diagnose with AI-assistance (AI-assisted trial) for the latter after certain minimum break time. For the rest half of the pathologists were asked to diagnose each trials in reverse. Detailed observer test design and results are illustrated in Fig. 4.

We observed that pathologist performance of AI-assisted trials exceeded that of pathologist-

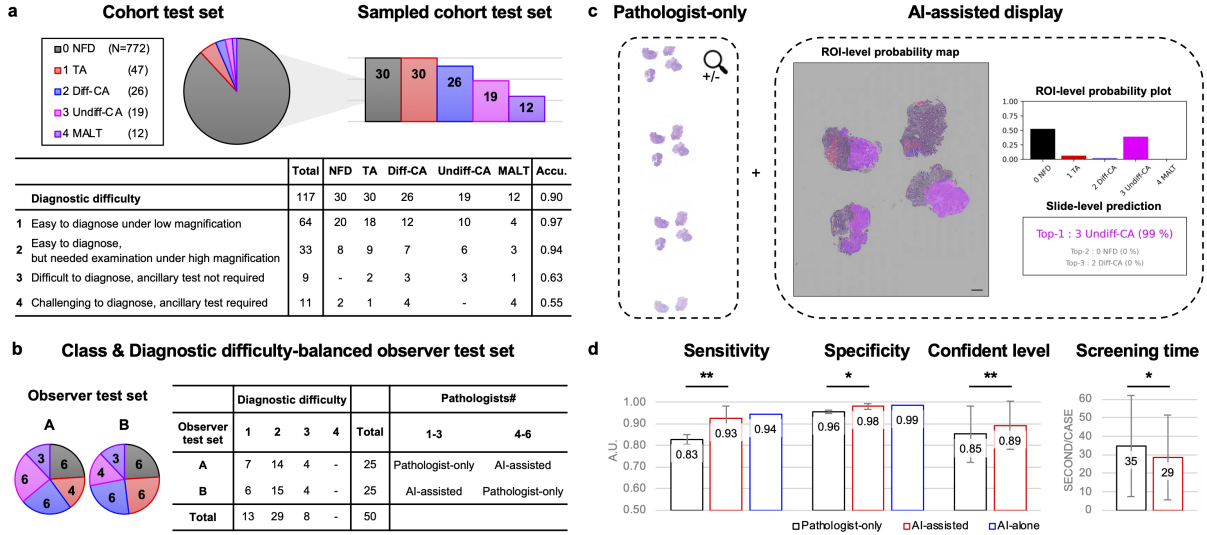


Figure 4: Observer study. (a) Diagnostic difficulty analysis of the sampled cohort test set. (b) Preparation of class and diagnostic difficulty-balanced observer test set. (c) Schematic of pathologist-only and AI-assisted trials. (d) Observer study results for each pathologist-only, AI-assisted and AI-alone trials.

only trials for all metrics with statistically significant level. As shown in Supplementary Table S4, the average sensitivity and specificity were increased by 0.10 and 0.02 with p-value of 0.006 and 0.015, respectively (sensitivity from 0.83 ± 0.02 to 0.93 ± 0.06 and specificity from 0.96 ± 0.01 to 0.98 ± 0.01). We found that the improved performance was achieved under higher confident level of the diagnosis within shorter screening time. The AI-assisted diagnostic confident level for each diagnosis improved by 0.04 with p-value of 0.007 (macro averaged confident level per WSI from 0.85 ± 0.13 to 0.89 ± 0.11). The AI-assisted trial saved screening time by 6.27 seconds per each WSI with p-value of 0.030 (micro averaged screening time per WSI from 34.80 ± 27.24 to 28.53 ± 23.15). The stand-alone AI performance (AI-alone trial) on both observer test sets was comparable to that of AI-assisted pathologist, and even exceeded pathologist-only trials by 0.12 and 0.03 for sensitivity and specificity, respectively.

We further compared pathologist and stand-alone AI performance using class-wise AI receiver operating characteristics (ROC) curves over the entire cohort tests, as shown in Fig. 5.

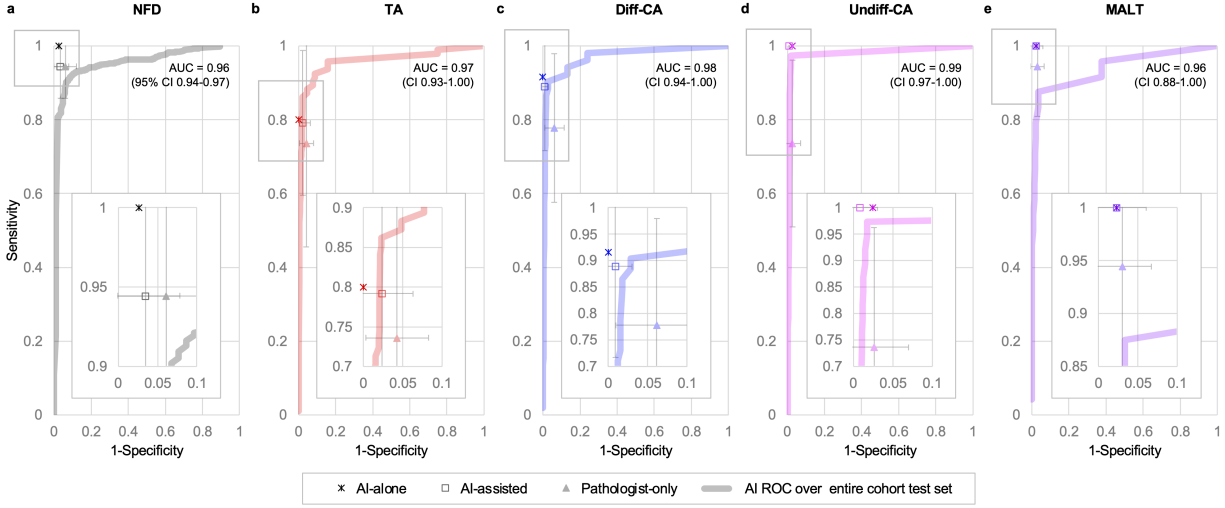


Figure 5: Class-wise ROC curve and observer test results. ROC curve represents the entire cohort test set performance and dot plot represents observer test performance for each AI-alone, AI-assisted and Pathologist-only trials. (a) NFD. (b) TA. (c) Diff-CA. (d) Undiff-CA. (e) MALT class.

Pathologist performance assisted by the AI system for all the classes improved toward upper-left side of the curve near the AI-alone performance. We further discovered that the AI system helped pathologists make performance more consistent. The AI-assisted pathologist performance over all classes showed less variation compared to pathologist-only performance, as depicted as error bar of each trials.

Discussion

The pathologic diagnosis of the GC are commonly classified by the digestive system of the world health organization (WHO) classification¹⁴. GC WHO classification endorses many histologic subtypes, however, the performance of existing AI systems tends to degrade when subdivided classes sharing similar histologic characteristics are not properly clustered. Hence, previous studies utilizing AI mostly adopt binary classification between benign versus malignant⁶, or differentiating gastric adenoma and carcinoma to non-neoplastic cases⁷⁻⁹. Our pathologic diagnosis of 5 subclassification of GC including MALT lymphoma is firstly tried by the proposed AI system. The AI

system achieves the proposed 5 subclassification accuracy that is almost close to pathology diagnosis over daily endoscopic cohort sets (Supplementary Table S3). Specifically, MALT lymphoma has a relatively high prevalence in East Asia related with high *Helicobacter pylori* (*H. pylori*) infection¹⁵. In South Korea, 1-2% of patients receiving upper endoscopic biopsy are classified as MALT lymphoma, and it corresponds to 12% of patients who diagnosed as gastric malignancy¹⁶. Diagnosis of MALT lymphoma largely depends on the pathologic confirmation, thus classification of MALT class should be listed on the gastric cancer screening program, especially in countries with high infection rates of *H. pylori*. Histologic features of MALT lymphoma help to diagnose the disease; however, diagnosis of MALT lymphoma is a challenge even for the pathologist and requires ancillary test, such as immunohistochemistry or molecular evaluation, due to its morphologic similarities with other inflammatory or tumorous diseases¹⁷. The AI system's AUC for MALT class (0.96 [95% CI, 0.88–1.00] and 0.99 [CI, 0.94–1.00] for internal and external cohort test, respectively) demonstrates its capability for guiding clinician to proceed additional evaluation for the *H.pylori* infection.

Specifically, the proposed classification categories GC into differentiated and undifferentiated carcinoma. Undifferentiated-type carcinoma is reported to have high incidence of lymph node metastasis^{18,19}; thus, identifying undifferentiated carcinoma is important for deciding surgical treatment²⁰. A recent work reported sequential application of a differentiated/undifferentiated binary classifier on a normal/tumor classifier result¹⁰. However, its relatively poor performance of undifferentiated carcinoma (AUC of 0.91 and 0.88 for internal and external test set, respectively) indicated the difficulty of discriminating confusing differentiated and undifferentiated cancer cells.

In fact, differentiating confusing adjacent classes, e.g., differentiated/undifferentiated and adenoma/adenocarcinoma, needs comprehensive understanding of structural characteristics. CNN-based patch-wise training has difficulty in understanding structural relationship between non-adjacent patches due to limited receptive field size. On the other hand, pathologists differentiate

confusing classes based on comprehensive information screened by switching magnification to check from regional-level features to global-level structural relationships. To mimic the way how pathologist understand WSIs, we therefore proposed hybrid architecture where CNN feature extractor is followed by ViT so that ViT can model long-range dependency among non-adjacent patch features after short-range dependency exploited by convolution kernels. As shown in Supplementary Fig. S1 and Supplementary Table S5, ROI-level probability map of the proposed CNN+ViT model provide less confusing prediction between patches within tissues compared to that of the CNN model, with statistically improved patch-level accuracy of 0.85 ± 0.06 compared to that of CNN of 0.79 ± 0.11 (p-value of <0.001). Based on improved ROI-level prediction results, our system successfully classify TA/Diff-CA/Undiff-CA, with average diagnostic sensitivity of above 0.80 for both internal and external cohort dataset.

Our AI system is not free of limitations. As shown in Fig. 5, the AI system ROC performance for TA, Diff-CA and Undiff-CA exceeds average performance of human pathologists. However, for NFD and MALT, average human pathologist performance exceeds the AI system ROC performance. One reasonable solution for improving degraded class performance may be matching class-wise distribution between training data set and daily cohort test set. For example, the number of inflammatory tissues of NFD, i.e., hyperplastic polyp or gastritis, may not be enough in the curated training dataset. More specifically, NFD distribution of the internal training dataset (15%) showed significant gap from that of the daily-acquired cohort test set (88%). Similarly, daily cohort test sets contain relatively increased rate of MALT cases that require ancillary test. The training dataset has a significantly lower proportion of uncertain cases of MALT lymphoma requiring further ancillary test. If our AI system would be trained with large number of inflammatory tissues or samples required ancillary test, it may have predicted samples of daily endoscopic screening dataset with reliable performance. Second, inter-centre stain variation may cause increased false-positive rate (18%) compared to the internal test results (10%). This generalizability issue may be alleviated by developing advanced data augmentation and stain normalization techniques or

training the system with multi-centre dataset.

Despite aforementioned limitations, our AI system has strong point in providing explainable ROI-level probability map together with the slide-level prediction. As shown in Fig. 3a, c and f, pathologists can refer ROI-level probability map to double-check suspicious inflammatory regions, especially when the ROI-level probability distribution is non-dominant or the slide level probability is uncertain. Moreover, for region marked as suspicious for MALT class, as shown in Fig. 3f, pathologist can proceed ancillary test to confirm the final diagnosis of MALT lymphoma.

Finally, it should be noted that the results of the observer test show the stand-alone AI performance exceeds the average performance of human pathologists for all classes. In our experiments, the observer's test set was curated after excluding samples that, due to the highest diagnostic difficulties, pose a challenge even to pathologists and require additional testing. Thus, for majority of WSIs with average level of diagnostic difficulty, the AI system can be directly utilized. For samples with uncertain probability or samples predicted as certain class considering the class-wise AI system performance, the diagnostic results may be further confirmed by expert pathologists.

Previous AI assistance system were developed as a preanalytic tool for early attention of the suspicious lesion in the cases and give second opinion to the pathologists. With our AI system performance, clinicians can receive a presumptive pathologic opinion for predicting the treatment and prognosis. Integrating AI system within the diagnostic workflow would be benefit of decreasing workloads on pathologists, practical aid for the surgical diagnosis, and can also provide diagnosis services for regions that have shortages in access to pathologists.

Methods

Annotation of data set. For our retrospective study, a total of 2440 hematoxylin and eosin (H&E) stained slides were collected from the archives of CNUH and CNUSH and were scanned with

a Pannoramic 250 (3DHISTECH) with x40 magnification. For the internal dataset, an expert pathologist annotated ROI-level labels and all the annotated regions are grouped into 5 classes. As shown in Table 1, cases with negative for any tumorous condition and background pixels were classified as NFD. Cases with low to high grade dysplasia were classified as TA. Malignant tumor was divided into Diff-CA, Undiff-CA, and MALT lymphoma. Diff-CA and Undiff-CA were classified by following Japanese classification guideline that was suggested for endoscopic resection²¹. Diff-CA included well to moderately differentiated tubular/papillary adenocarcinoma, and Undiff-CA included poorly differentiated tubular/poorly cohesive/signet ring cell (SRC)/mucinous adenocarcinomas. MALT class was diagnosed followed by Wotherspoon criteria which was score 4 or above²².

For all the datasets, slide-level diagnosis was conducted given ROI-level analysis over entire WSI by an expert pathologist. For confusing cases, consensus was made by more than 2 pathologists.

AI system. Inspired by the success of ViT for image classification task, we utilized ViT as backbones of our AI system. Vision Transformer (ViT), introduced in computer vision community by learning long-range dependency between word tokens through self-attention, showed state-of-the-art (SOTA) performance in various vision tasks²³. We adapted ViT architecture to learn long-range structural dependency between patches within histopathological images by attending diagnostically important areas.

As depicted in Supplementary Fig. S2, the AI system was composed of ROI-level and slide-level networks. The ROI-level network was composed of CNN and the stage-1 ViT module. The CNN module was utilized as feature extractor, thus ResNet-50 pre-trained with large number of ImageNet dataset was used²⁴. The ViT module was employed to learn inter-patch relationships through inter-patch attention, and ViT-B pre-trained with ImageNet dataset was used¹³. More

specifically, as illustrated in Supplementary Fig. S2a, for ROI-level prediction, an input patch stack was stain normalized and fed into the ImageNet pre-trained CNN. The CNN extracted low-level features of each patch in the stacks, resulting in a 8×8 grid 2-D feature map with the feature dimensions of 2048. Each features represents 256×256 -pixel patch unit in the input patch stack. The extracted features for each patch were then flattened and embedded with embedding dimension of 768, in preparation for matching input dimension for the pre-trained ViT-B model. The embedded patches added by positional embeddings were then fed into the transformer encoder composed of successive self-attention layers. The encoded transformer output features were then linearly projected to have feature dimension of total number of classes, and reshaped into its original 2D-feature map dimension to be matched with their corresponding patch-level ground truths. For patches when training the ROI-level network, we applied geometric augmentation including random rotating, flipping and scaling with additional data augmentation techniques following BYOL²⁵ (color jittering, gaussian blurring and solarization). The optimal parameters for network training conditions were determined experimentally (see Supplementary Table. S5).

The slide-level network was composed of the stage-2 ViT module, pre-trained with ImageNet dataset. As depicted in Supplementary Fig. S2b, the slide-level network took intermediate features encoded from the stage-1 ViT over an entire slide, which had been inferenced with frozen ROI-level network weights, as shown in Supplementary Fig. S2b. We expanded input receptive field of the stage-2 ViT to cover entire gigapixel-level WSI by applying a max pooling 3×3 adjacent patches. The pooled input features were then flattened to be fed into the stage-2 ViT-B model. We then prepended learnable class token with identical feature dimension in front of the flattened feature array, resulting the class embedding that attended to entire feature embeddings throughout the successive self-attention layers. The encoded output feature of the class token was then linearly projected to have feature dimension that matches the total number of classes. For providing clinician-friendly results, the final output was converted to probability score from 0 to 100% by using Softmax function.

In order to adjust false-positive rate gap between the training dataset and other test sets, we adapted a minimum cut-off threshold of 0.03 for the ROI-level probability. The slide-level top-1 class was regarded as true-positive when its corresponding ROI-level probability was above the cut-off threshold, i.e., diagnosis with significantly low ROI-level probability was regarded as false-positive prediction. The optimal threshold for ROI-level offset were determined experimentally.

Implementation. For training the ROI-level network, batch size was set 4 and the model was trained for 30 epochs with the initial learning rate of 0.00001. For optimizing the ROI-level network training, we used Adam with decoupled weight decay (AdamW) optimizer with cosine scheduler for learning rate and weight decaying rate. For training the slide-level network, batch size was set 5 and the model was trained for 50 epochs with initial learning rate of 0.0004. For optimizing the slide-level network training, we used the stochastic gradient descent (SGC) optimizer with cosine scheduler for learning rate. For training both the ROI-level and slide-level networks, output predictions were trained to match its corresponding one-hot encoded logits by minimizing class weighted cross entropy (CE) loss. The optimal hyper parameters were determined experimentally. All the experiments were performed using Python version 3.9 and Pytorch library version 1.10 on a Nvidia RTX 3090 GPU.

Observer study design. The observer study was designed to evaluate the AI-assisted pathologist performance on daily gastric endoscopic screening. As shown in Fig. 4a-b, on 117 cases of the sampled cohort test set, two observer test set ($n = 25/\text{set}$) were prepared considering distribution of class and diagnostic difficulty level. We excluded cases with the highest diagnostic difficulty, for avoiding potential diagnostic disagreement. All the participants were given documented AI system performance and classification guidelines justified by an expert pathologist participated in the annotation process. For each test set, participants were given 25-minutes of time constraints and screening time for each case was recorded. Neither case revision nor answer correction was restricted. Minimum 3-hours of break time was given between each test sets. The order

of pathologist-only and AI-assistance trial was pre-determined by defining 2 test groups according to the pathologist ID. Total 6 pathologists from CNUH and CNUSH were participated in the observer test. Among the participants, 4 pathologists of over 10 years of experience were equally split into different test groups. A pathologist of over 5 years of experience and a pathology resident of over 4 years of experience were split into different test groups.

Participants were given 5 sample cases to simulate the AI-assisted test prior to the main test. Participants were then asked to diagnose WSIs in each observer test set with (AI-assisted) and without AI-assistance (Pathologist-only), respectively. For the pathologist-only trial, raw data files from each test set were pre-uploaded on SlideViewer 2.5 (3DHISTECH) software and participants were allowed to utilize all the built-in functions of the software. For the AI-assisted trial, pre-processed AI system results composed of ROI-level and slide-level outputs, were provided on an additional monitor, as illustrated in Fig. 4c. The participants were asked to fill out answers in tables (Excel 2019, Microsoft), and asked to score their confident level of the diagnosis from least (0) to most (1.00) for each case. Confident level of the diagnosis was justified as follows: indefinite for, <0.50; suspicious for, 0.51-0.70; favor, 0.71-0.80; consistent with, 0.81-0.90; diagnostic of, 0.91-1.00, following ²⁶.

Metrics. For evaluating the ROI-level network performance, we utilized patch-level accuracy per each WSI. The metric is defined as follows:

$$Accuracy_{patch}(y, \hat{y}) = \frac{1}{|S_c|} \sum_{s \in S_c} \left(\frac{1}{|P_s|} \sum_{p \in P_s} M_p \cdot 1(\hat{y}_p = y_p) \right),$$

where S_c is the set of WSI samples of each slide-level ground truth class, P_s is the set of patches within s -th WSI sample, \hat{y}_p is the predicted value of the p -th patch and y_p is the corresponding patch-level annotation label, and M_p is foreground mask, which is set to 1 when a patch consists of more than 10% of foreground pixels.

For evaluating the slide-level network performance of the stage-2 network, we utilized class-wise slide-level AUC (area under the ROC curve), Accuracy, Precision, Specificity and Sensitivity. These metrics are defined as follows:

$$\begin{aligned}
Accuracy &= \frac{tp + tn}{tp + tn + fp + fn}, \\
Precision &= \frac{tp}{tp + fp}, \\
Specificity &= \frac{tn}{tn + fp}, \\
Sensitivity &= \frac{tp}{tp + fn},
\end{aligned}$$

where tp, tn, fp, fn represent true positive, true negative, false positive, false negative cases for each class, respectively. All the metrics were by calculated using Scikit-learn package²⁷.

For averaging multi-class metrics or multi-observer test metrics, we utilized macro average as default. The metric is defined as follows:

$$Average = \frac{1}{|C|} \sum_{c \in C} O_c,$$

where C is the set of slide-level ground truth classes and O_c represents any class-wise performance metric, e.g., AUC, Accuracy, precision, Specificity and Sensitivity.

For averaging entire observer test records, e.g., confident level of the diagnosis and screening time, we utilized micro average. The metric is defined as follows:

$$Average(micro) = \frac{1}{|S|} \sum_{s \in S} s,$$

where S is the set of observer test records over all the participants.

Statistical analysis. Statistical analysis for the observer test was performed using MATLAB R2020a (Mathworks, Natick). Kolmogorov Smirnov test was used to evaluate normality of all the results. Since all the test results were non-normally distributed, a two-sided Wilcoxon rank sum test was used to stastically compare performance metrics. p-value was utilized as statistical significance level and indicated as asterisks, i.e., * for $p < 0.05$; ** for $p < 0.01$.

Ethical approval. This study was approved by the institutional review board of CNUH (IRB file no. 2021-10-028) and CNUSH (IRB file no. 2021-12-004), which waived the requirement for informed consent. All slides were provided by the Biobank of CNUH, a member of the Korea Biobank Network.

Correspondence Correspondence and requests for materials should be addressed to Min-Kyung Yeo (email: mkyeo83@cnu.ac.kr) and Jong Chul Ye (email: jong.ye@kaist.ac.kr).

Acknowledgements This work was supported by the National Research Foundation (NRF) of Korea grant NRF-2020R1A2B5B03001980 and the Institute of Information & communications Technology Planning & Evaluation (IITP) grant funded by the Korea government (MSIT) (No.2019-0-00075, Artificial Intelligence Graduate School Program (KAIST)). This work was also supported by Korea Health Technology R&D Project through the Korea Health Industry Development Institute (KHIDI), funded by the Ministry of Health & Welfare, Republic of Korea (grant number: HR20C0025).

Author Contributions Y.O. performed all experiments, wrote the extended code, and prepared the manuscript. G.E.B and K.H.K collected and labeled data. M.K.Y collected and labeled data, supervised the project in conception and discussion, and prepared the manuscript. J.C.Y. supervised the project in conception and discussion, and prepared the manuscript.

Competing Interests The authors declare that they have no competing financial interests.

References

1. Sung, H. *et al.* Global cancer statistics 2020: Globocan estimates of incidence and mortality worldwide for 36 cancers in 185 countries. *CA: a cancer journal for clinicians* **71**, 209–249 (2021).
2. Jun, J. K. *et al.* Effectiveness of the korean national cancer screening program in reducing gastric cancer mortality. *Gastroenterology* **152**, 1319–1328 (2017).
3. Jiang, Y., Yang, M., Wang, S., Li, X. & Sun, Y. Emerging role of deep learning-based artificial intelligence in tumor pathology. *Cancer Communications* **40**, 154–166 (2020).
4. Bulten, W. *et al.* Automated deep-learning system for gleason grading of prostate cancer using biopsies: a diagnostic study. *The Lancet Oncology* **21**, 233–241 (2020).
5. Bejnordi, B. E. *et al.* Diagnostic assessment of deep learning algorithms for detection of lymph node metastases in women with breast cancer. *Jama* **318**, 2199–2210 (2017).
6. Song, Z. *et al.* Clinically applicable histopathological diagnosis system for gastric cancer detection using deep learning. *Nature communications* **11**, 1–9 (2020).
7. Yoshida, H. *et al.* Automated histological classification of whole-slide images of gastric biopsy specimens. *Gastric cancer* **21**, 249–257 (2018).
8. Park, J. *et al.* A prospective validation and observer performance study of a deep learning algorithm for pathologic diagnosis of gastric tumors in endoscopic biopsies. *Clinical Cancer Research* **27**, 719–728 (2021).
9. Iizuka, O. *et al.* Deep learning models for histopathological classification of gastric and colonic epithelial tumours. *Scientific reports* **10**, 1–11 (2020).

10. Jang, H.-J., Song, I.-H. & Lee, S.-H. Deep learning for automatic subclassification of gastric carcinoma using whole-slide histopathology images. *Cancers* **13**, 3811 (2021).
11. jgca@ koto. kpu-m. ac. jp, J. G. C. A. Japanese gastric cancer treatment guidelines 2018. *Gastric Cancer* **24**, 1–21 (2021).
12. Liu, Y. *et al.* Detecting cancer metastases on gigapixel pathology images (2017). 1703.02442.
13. Dosovitskiy, A. *et al.* An image is worth 16x16 words: Transformers for image recognition at scale. *arXiv preprint arXiv:2010.11929* (2020).
14. Nagtegaal, I. D. *et al.* The 2019 who classification of tumours of the digestive system. *Histopathology* **76**, 182 (2020).
15. Asenjo, L. & Gisbert, J. Prevalence of helicobacter pylori infection in gastric malt lymphoma: a sistematic review. *Revista Española de Enfermedades Digestivas* **99**, 398 (2007).
16. Yang, H.-J. *et al.* Management of suspicious mucosa-associated lymphoid tissue lymphoma in gastric biopsy specimens obtained during screening endoscopy. *Journal of Korean Medical Science* **31**, 1075–1081 (2016).
17. Bacon, C. M., Du, M.-Q. & Dogan, A. Mucosa-associated lymphoid tissue (malt) lymphoma: a practical guide for pathologists. *Journal of clinical pathology* **60**, 361–372 (2007).
18. Gotoda, T. *et al.* Incidence of lymph node metastasis from early gastric cancer: estimation with a large number of cases at two large centers. *Gastric cancer* **3**, 219–225 (2000).
19. Kook, M.-C. Risk factors for lymph node metastasis in undifferentiated-type gastric carcinoma. *Clinical endoscopy* **52**, 15 (2019).
20. Gotoda, T., Yamamoto, H. & Soetikno, R. M. Endoscopic submucosal dissection of early gastric cancer. *Journal of gastroenterology* **41**, 929–942 (2006).

21. jgca@koto.kpu-m.ac.jp, J. G. C. A. Japanese classification of gastric carcinoma: 3rd english edition. *Gastric cancer* **14**, 101–112 (2011).
22. Wotherspoon, A. C. *et al.* Regression of primary low-grade b-cell gastric lymphoma of mucosa-associated lymphoid tissue type after eradication of helicobacter pylori. *The Lancet* **342**, 575–577 (1993).
23. Khan, S. *et al.* Transformers in vision: A survey. *arXiv preprint arXiv:2101.01169* (2021).
24. He, K., Zhang, X., Ren, S. & Sun, J. Deep residual learning for image recognition. In *Proceedings of the IEEE conference on computer vision and pattern recognition*, 770–778 (2016).
25. Grill, J.-B. *et al.* Bootstrap your own latent-a new approach to self-supervised learning. *Advances in Neural Information Processing Systems* **33**, 21271–21284 (2020).
26. Lindley, S. W., Gillies, E. M. & Hassell, L. A. Communicating diagnostic uncertainty in surgical pathology reports: disparities between sender and receiver. *Pathology-Research and Practice* **210**, 628–633 (2014).
27. Pedregosa, F. *et al.* Scikit-learn: Machine learning in Python. *Journal of Machine Learning Research* **12**, 2825–2830 (2011).
28. Deng, J. *et al.* Imagenet: A large-scale hierarchical image database. In *2009 IEEE conference on computer vision and pattern recognition*, 248–255 (Ieee, 2009).
29. Ciga, O., Xu, T. & Martel, A. L. Self supervised contrastive learning for digital histopathology. *Machine Learning with Applications* **7**, 100198 (2022).

Table 1: Gastric cancer histology classification for guiding early gastric cancer treatment

5 class classification of gastric cancer histology		Gastric cancer treatment guidance
0 NFD	Negative for Dysplasia	- Follow-up biopsy - Observation
1 TA	Tubular Adenoma	- Endoscopic (sub)mucosal dissection - Observation and follow-up
2 Diff-CA	Differentiated Carcinoma	- Endoscopic submucosal dissection according to the indication - Surgical resection
3 Undiff-CA	Undifferentiated Carcinoma	- Surgical resection
4 MALT	MALT lymphoma	- H.Pylori eradication - Radiation, Chemotherapy

Supplementary Materials

Supplementary Table S1: Class distribution of the internal, cohort test and external dataset.

Class	a Internal dataset								b Cohort test set		c External dataset	
	# of slides		Train set		Validation set		Test set		Test set		Test set	
			# of patch stacks	%	# of slides	%	# of slides	%	# of slides	%	# of slides	%
0 NFD	263	31	1,850	15	38	28	73	30	772	88	297	88
1 TA	160	19	1,825	15	24	18	43	17	47	5	11	3
2 Diff-CA	175	21	2,977	24	31	23	54	22	26	3	12	4
3 Undiff-CA	180	21	5,032	40	33	24	58	23	19	2	8	2
4 MALT	68	8	826	7	9	7	19	8	12	1	8	2
Total	846		12,510		135		247		876		336	

Supplementary Table S2: Class-wise classification performance of the AI system.

a Internal test set

Class	ROI-level	AUC [95% CI]	Slide-level			
	$Accuracy_{patch}$		Accuracy	Precision	Specificity	Sensitivity
0 NFD	0.97	0.99 [0.97, 1.00]	0.96	1.00	1.00	0.88
1 TA	0.82	0.99 [0.97, 1.00]	0.97	0.89	0.98	0.93
2 Diff-CA	0.79	1.00 [0.98, 1.00]	0.97	0.93	0.98	0.93
3 Undiff-CA	0.87	1.00 [0.98, 1.00]	0.97	0.89	0.96	1.00
4 MALT	0.83	1.00 [0.98, 1.00]	0.98	0.89	0.99	0.89
Average	0.85 ± 0.07	0.99 ± 0.00	0.97 ± 0.01	0.92 ± 0.05	0.98 ± 0.01	0.93 ± 0.05

b Cohort test set

Class	ROI-level	AUC [95% CI]	Slide-level			
	$Accuracy_{patch}$		Accuracy	Precision	Specificity	Sensitivity
0 NFD	-	0.96 [0.94, 0.97]	0.89	0.99	0.95	0.89
1 TA	-	0.97 [0.93, 1.00]	0.95	0.51	0.95	0.89
2 Diff-CA	-	0.98 [0.94, 1.00]	0.97	0.46	0.97	0.88
3 Undiff-CA	-	0.99 [0.97, 1.00]	0.97	0.42	0.97	1.00
4 MALT	-	0.96 [0.88, 1.00]	0.98	0.36	0.98	0.67
Average	-	0.97 ± 0.02	0.95 ± 0.04	0.59 ± 0.24	0.97 ± 0.02	0.87 ± 0.12

c External dataset

Class	ROI-level	AUC [95% CI]	Slide-level			
	$Accuracy_{patch}$		Accuracy	Precision	Specificity	Sensitivity
0 NFD	-	0.89 [0.85, 0.93]	0.82	1.00	0.97	0.80
1 TA	-	0.95 [0.87, 1.00]	0.94	0.32	0.95	0.73
2 Diff-CA	-	0.96 [0.88, 1.00]	0.93	0.31	0.94	0.75
3 Undiff-CA	-	0.97 [0.88, 1.00]	0.88	0.17	0.88	1.00
4 MALT	-	0.99 [0.94, 1.00]	0.96	0.40	0.96	1.00
Average	-	0.95 ± 0.04	0.92 ± 0.06	0.50 ± 0.30	0.96 ± 0.03	0.86 ± 0.13

Supplementary Table S3: Detailed classification performance of the AI system. Underlined items indicate correct predictions.

a Cohort test set (N=876)

Detailed classification	AI system prediction					Total	AI system prediction (per row percentile, %)				
	0 NFD	1 TA	2 Diff-CA	3 Undiff-CA	4 MALT		0 NFD	1 TA	2 Diff-CA	3 Undiff-CA	4 MALT
Negative for dysplasia											
- Foveolar hyperplasia	<u>10</u>					10	<u>100</u>				
- Hyperplastic polyp	<u>44</u>	3		7		54	<u>81</u>	6		13	
- Acute gastritis	<u>193</u>	11	9	10	9	232	<u>83</u>	5	4	4	4
- Atrophic gastritis	<u>438</u>	25	6	6	1	476	<u>92</u>	5	1	1	<1
Tubular Adenoma (TA)											
- TA, Low grade	2	<u>41</u>	1		1	45	4	<u>91</u>	2		2
- TA, High grade		<u>1</u>	1			2		<u>50</u>	50		
Differentiated carcinoma ; Tubular adenocarcinoma (TAC)											
- TAC, Well differentiated		2	<u>9</u>			11		18	<u>82</u>		
- TAC, Moderately differentiated			<u>14</u>	1		15			<u>93</u>	7	
Undifferentiated carcinoma											
- TAC, Poorly differentiated				<u>14</u>		14				<u>100</u>	
- Poorly cohesive carcinoma				<u>3</u>		3				<u>100</u>	
- Signet ring cell carcinoma				<u>2</u>		2				<u>100</u>	
MALT											
- MALT lymphoma	3			1	<u>8</u>	12	25			8	<u>67</u>
Total						876					

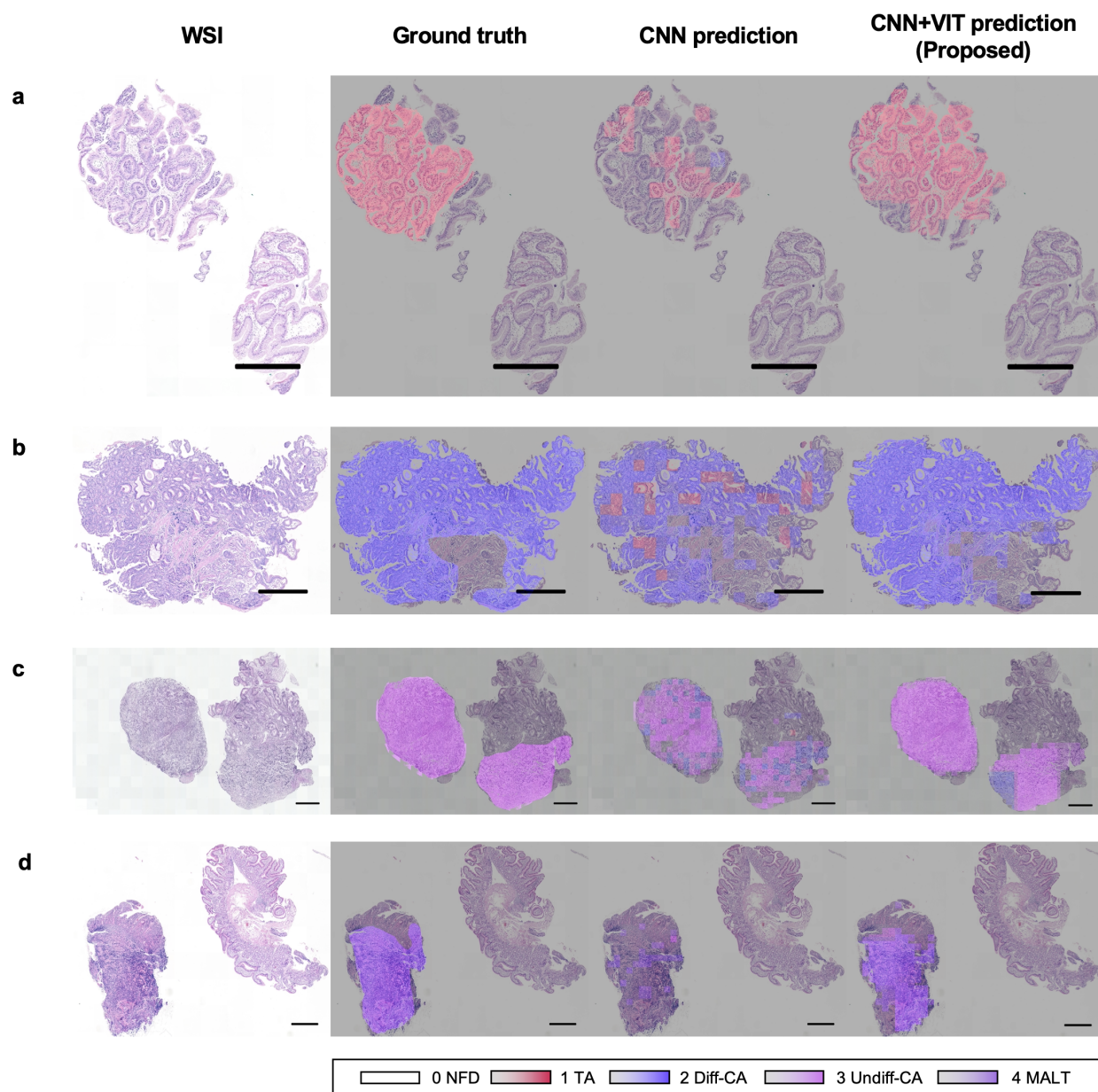
b External test set (N=337)

Detailed classification	AI system prediction					Total	AI system prediction (per row percentile, %)				
	0 NFD	1 TA	2 Diff-CA	3 Undiff-CA	4 MALT		0 NFD	1 TA	2 Diff-CA	3 Undiff-CA	4 MALT
Negative for dysplasia											
- Foveolar hyperplasia	<u>4</u>					4	<u>100</u>				
- Hyperplastic polyp	<u>8</u>	1		1		10	<u>80</u>	10		10	
- Acute gastritis	<u>84</u>	6	6	17	9	122	<u>69</u>	5	5	14	7
- Atrophic gastritis	<u>142</u>	7	3	9		161	<u>88</u>	4	2	6	
Tubular Adenoma (TA)											
- TA, Low grade	1	<u>6</u>	1			8	13	<u>75</u>	13		
- TA, High grade		<u>2</u>	1			3		<u>67</u>	33		
Differentiated carcinoma ; Tubular adenocarcinoma (TAC)											
- TAC, Well differentiated			<u>2</u>			2			<u>100</u>		
- TAC, Moderately differentiated		1	<u>7</u>	2		10		10	<u>70</u>	20	
Undifferentiated carcinoma											
- TAC, Poorly differentiated				<u>5</u>		5				<u>100</u>	
- Poorly cohesive carcinoma				<u>3</u>		3				<u>100</u>	
- Signet ring cell carcinoma											
MALT											
- MALT lymphoma					<u>8</u>	8					<u>100</u>
Others (excluded)											
- Diffuse large B-cell lymphoma				1		1				100	
Total						337					

Supplementary Table S4: Detailed observer test results.

Trial		Pathologists						AI	Average (micro)	Improvement (w.r.t pathologist-only)	p-value
		1	2	3	4	5	6				
Pathologist-only	Observer test set	A	A	A	B	B	B				
	Accuracy	0.88	0.80	0.84	0.80	0.84	0.80		0.83 ± 0.03		
	Sensitivity	0.85	0.83	0.83	0.80	0.85	0.80		0.83 ± 0.02		
	Specificity	0.97	0.95	0.96	0.95	0.96	0.95		0.96 ± 0.01		
	Confident level (a.u.)	0.76	0.78	0.87	0.85	0.89	0.96		(0.85 ± 0.13)		
	Screening time (s/WSI)	41.12	47.44	47.88	22.56	36.2	13.6		(34.80 ± 27.24)		
AI-assisted	Observer test set	B	B	B	A	A	A				
	Accuracy	1.00	0.96	0.92	0.92	0.88	0.84		0.92 ± 0.06	+0.09	0.015
	Sensitivity	1.00	0.97	0.93	0.93	0.87	0.85		0.93 ± 0.06	+0.10	0.006
	Specificity	1.00	0.99	0.98	0.98	0.97	0.96		0.98 ± 0.01	+0.02	0.015
	Confident level (a.u.)	0.85	0.80	0.90	0.91	0.95	0.95		(0.89 ± 0.11)	+0.04	0.007
	Screening time (s/WSI)	20.56	34.52	44.24	20.16	35.84	15.88		(28.53 ± 23.15)	-6.27	0.030
AI-alone	Observer test set							A+B			
	Accuracy							0.94		+0.11	
	Sensitivity							0.94		+0.12	
	Specificity							0.99		+0.03	

(a.u., arbitrary unit; s/WSI, second per whole slide image)

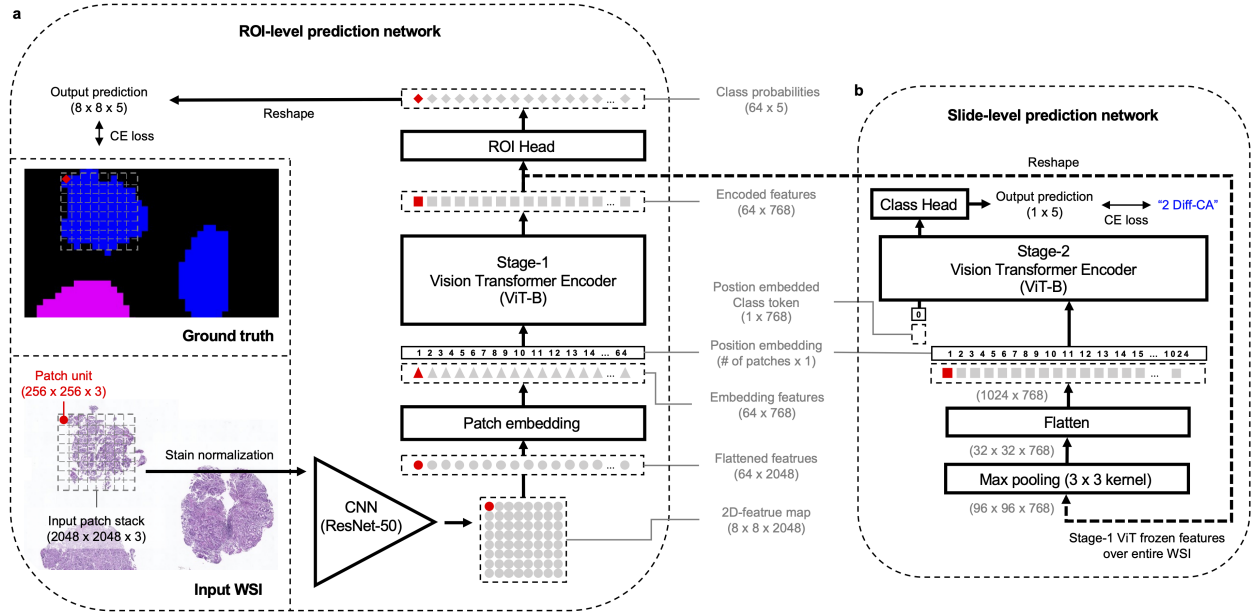


Supplementary Figure S1: ROI-level probability map comparison between CNN and CNN+ViT frameworks. Representative cases selected from (a) TA, (b) Diff-CA, (c) Undiff-CA and (d) MALT class. All the scale bars indicate 500 μm .

Supplementary Table S5: Model performance comparison.

Model ROI-level	Training condition					a Internal test set ROI-level <i>Accuracy_{patch}</i>	b Cohort test set Slide-level				c External dataset Slide-level			
	Magn.	Resolution ($\mu\text{m}/\text{pixel}$)	Receptive field ($\text{H} \times \text{W}$, mm)	CNN pretraining Dataset	Method		AUC	Accu.	Spec.	Sens.	AUC	Accu.	Spec.	Sens.
CNN+ViT	$\times 5$	1.95	2×2	IM	Supervised	0.84 ± 0.07	0.94	0.94	0.95	0.82	0.91	0.91	0.93	0.80
	$\times 10$	0.97	1.5×1.5	IM	Supervised	0.85 ± 0.08	0.94	0.96	0.97	0.86	0.92	0.92	0.93	0.75
	$\times 20$	0.49	1×1	IM PA	Supervised SimCLR	0.85 ± 0.06 0.81 ± 0.10	0.97 0.95	0.95 0.94	0.97 0.96	0.87 0.79	0.95 0.93	0.92 0.89	0.96 0.94	0.86 0.77
CNN	$\times 20$	0.49	0.13×0.13	IM	Supervised	0.79 ± 0.11	-	-	-	-	-	-	-	-

(Magn., magnification ratio; IM, ImageNet²⁸; PA, Pathology dataset collected from multiple-organs²⁹; Accu., Accuracy; Spec., Specificity; Sens., Sensitivity)



Supplementary Figure S2: Overall architecture of the AI system. (a) ROI-level prediction network with CNN+ViT backbone. The CNN extracts low-level features, and the ViT learns inter-patch relationships through self-attention mechanism. (b) Slide-level prediction network with ViT backbone. The ViT learn intermediate features encoded from the stage-1 ViT over an entire slide. CE, Cross-entropy; WSI, whole slide image.